

# **Evaluating surface heat flux in planar water-jet cooling of moving hot solid by inversely solving steady-state heat conduction**

Tokuma Hikata and Hitoshi Fujimoto\*

Department of Energy Science and Technology, Graduate School of Energy Science, Kyoto University, Kyoto 606-8501, Japan.

\* Corresponding author:– [fujimoto.hitoshi.3x@kyoto-u.ac.jp](mailto:fujimoto.hitoshi.3x@kyoto-u.ac.jp)

## **Abstract**

In steel-manufacturing industries, water-jet quenching of a moving hot solid is commonly used for run-out table cooling in hot rolling mills. Hence, the evaluation of the surface heat flux in the jet-impact region is necessary for precise temperature control. In this study, we developed an evaluation method for surface heat flux in the impact region by inversely solving the steady-state heat-conduction equation, considering the temperature profile on the reverse side of jet impingement. The main advantage was that the heat-flux distribution could be evaluated with a high spatial resolution. The developed method was validated using the exact solution of the heat-conduction equation. The inverse analysis was highly sensitive to the numerical scheme and small errors in the temperature profile on the reverse side. An appropriate numerical scheme and smoothing operation of the temperature profile allowed the reasonable evaluation of surface heat flux on the cooled surface. In addition, the developed

method was applied to laboratory-scale cooling experiments to confirm its applicability. The heat-transfer characteristics of planar jet impinging on a moving solid were studied in the conditions that the temperature of the solid with 0.5 mm thickness was 200–600 °C, and its velocity was 1.5, 3.0, and 4.4 m/s. The heat flux in the jet-impact region depended significantly on these parameters.

**Keywords:** Inverse heat conduction, water jet cooling, heat flux, moving solid

## 1. Introduction

Jet cooling of hot materials is prevalent in several industrial applications, including cooling electronic components [1], glass tempering [2], and quenching of the reactor core in nuclear plants [3]. In steel manufacturing, water-jet quenching is commonly used during heat treatment to harden the steel products [4–8]. Water-jet impingement is also used on hot, moving steel for continuous mass production. For example, in rolling mills, hot steel sheets in motion are rapidly cooled using water-jet arrays on a runout table (ROT) [9], as shown in Figure 1. Evaluating the heat-transfer rate between the hot, moving solids and the cooling jets with high accuracy and spatial resolution is a key challenge in ROT cooling processes for improving heat control in industries.

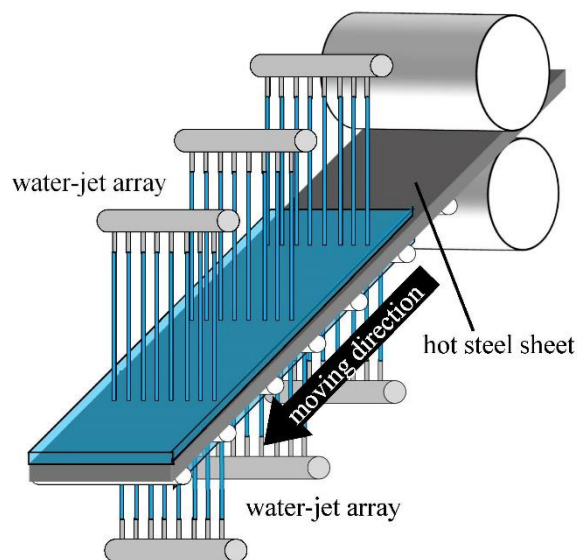


**Figure 1** Schematic of run-out table cooling

Four types of experiments have been conducted to study the heat-transfer rate of free-surface jet impingement onto a moving, hot solid. The first type uses a pilot plant or actual cooling system in a commercial mill [9–12]. An industry-scale setup is suitable for obtaining practical heat-transfer data. The second type is water-jet impingement onto a rotating cylinder [3, 13–15]. Unlike ROT cooling, the jet impinges onto a non-flat solid surface. The advantage of this method is that the velocity of the solid and rate of jet impingement can be varied by adjusting the rotation speed of the cylinder. In addition, intermittent multi-jet impingements onto a hot, moving solid can be realized using a compact experimental setup. The third type involves free-surface jets impingements onto a moving flat solid mounted on a linear unit [16–18]. The hot solid is cooled using multi-jet impingement by repeatedly moving the solid backwards and forwards. The fourth type is similar to the third, but the jet is impinged onto the moving solid once [19]. The present study is based on this experiment type.

This research focused on developing an evaluation method for the surface heat flux as the jet cools the moving solid. In most studies [3, 9-11, 13-16, 18, 19], the inverse heat conduction problem (IHCP) was solved for evaluating surface heat flux. The temperature history of the moving solid was measured by thermocouples embedded in the solid or attached to the solid surface. The transient heat conduction equation has been inversely solved numerically or analytically by referring to the temperatures. Two-dimensional equations have been adopted in many works [3, 9, 10, 13-16, 18, 19], whereas three-

dimensional equations have been employed less frequently [11]. The accuracy and spatial resolution of the evaluated surface heat flux depends significantly on the number of temperature-measurement points (thermocouples). In theory, a large number of temperature-measurement points can help obtain the surface heat flux profile with a high spatial resolution and accuracy. However, in practice, it is difficult to set up that many thermocouples in a small space around a solid. This experimental difficulty prevents evaluation with a high spatial resolution. A significant gap exists between the literature and the actual industrial demand.

This issue can be solved using an infrared camera, which is a non-contact measurement device to capture the temperature profile with high spatial resolution. However, unlike thermocouples, an infrared camera cannot measure the temperature inside a metal solid. In addition, temperature measurement of a solid surface covered with water is difficult. An infrared camera can only measure the temperature profile of a dry solid surface. Note that the dry side of the steel plate may cool at a different rate. Moreover, noise-induced error reduces the accuracy of an infrared image sensor at high temperatures. Therefore, the utilization of infrared cameras is effective when thin solid sheets are used [20–22]. Nevertheless, we found the use of an infrared camera appealing for evaluating surface heat flux.

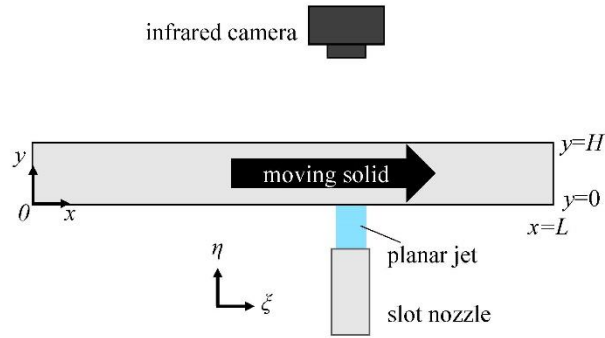


**Figure 2** Schematic of free-surface planar jet cooling of a moving hot solid

When a single water jet is cooling a solid moving at a constant velocity, as shown in Fig. 2, the infrared camera can be placed on the other side. Because of the constant movement, the duration of water contact is small at any particular point. The temperature distribution in the solid is almost independent of time for coordinates fixed in space. The heat flux of the cooled surface can be evaluated using the 3-dimensional steady-state heat conduction analysis, considering the temperature profiles on the reverse side [21, 22]. This solution method is significantly simpler than solving the transient heat conduction equation [19]. The surface heat flux with a high spatial resolution can be obtained easily. However, the quasi-steady method has been rarely studied compared to the transient-heat-conduction models. The applicability of quasi-steady models remains uncertain, and the method's validity has not yet been studied in detail.

The heat-transfer characteristics of a circular water-jet onto a hot, moving solid were investigated [21, 22]. The velocity of the solid was maintained below or equal to 1.5 m/s, and the solid's thickness 0.3 mm. The present authors found the evaluation method inapplicable to the planar-jet impingements

data for a larger velocity ( $\sim 4.4$  m/s) and thicker solid ( $\sim 0.5$  mm), as will be shown later. The fact suggests that further improvement is needed to expand the applicability range of the quasi-steady models.

The main objective of this study is to develop quasi-steady models for evaluating the heat-transfer rate, between a jet impingement and a hot, moving solid, with high-spatial resolution. The cooling method considered for this study had a planar, upward water jet impinging onto a moving hot solid, as shown in Figure 2. The temperature on the reverse side was measured using an infrared camera. Two types of models have been proposed: a simple model based on heat-energy conservation and the IHCP-based model using steady-state heat conduction equation by modifying the model in [21,22]. The latter model was the focus of this study. The solving method and filtering operation for removing measurement errors were thoroughly investigated. The models were validated by comparing the model evaluation and exact solution of the heat-conduction equation. Subsequently, a 3-D model was built and employed in laboratory-scale experiments, in which a planar jet cooled a 0.5 mm thick stainless steel sheet at 200–600 °C, at moving velocity of 1.5, 3.0, and 4.4 m/s. The validity of the developed method is discussed in practical perspectives. In addition, we experimentally studied how the solid's temperature and the plate's velocity affected the boiling-heat-transfer characteristics.

## 2. Outline of free-surface planar jet cooling and exact solutions of heat-conduction equation

Figure 2 shows the schematic of planar water-jet cooling of a moving, hot solid and the definitions of the coordinates considered in the present study. Two types of coordinates are defined: a 2-D Cartesian coordinate  $(\xi, \eta)$  fixed in space and a moving coordinate  $(x, y)$ , traveling at the same velocity  $(V_s)$  as the hot solid. The measured temperature profile obtained using an infrared camera is represented by the  $(\xi, \eta)$  coordinate system fixed in space. The temperature profile of the cooled (bottom) side is an unknown value in the inverse analysis.

The model's assumptions are expressed in coordinates  $(x, y)$ . The length of the hot solid plate,  $L$ , is significantly large compared to the thickness of the solid,  $H$ . Initially, the temperature of the solid is uniform  $(T_0)$ , and the water-jet cooling starts at time  $t = 0$ . The jet's initial impact point is away from the edges of the plate. On that surface  $y = 0$ , the cooling is intensive at the jet-impact region. The region shifts at a velocity  $-V_s$ , and the heat-transfer rate is negligibly small in the non-impact region. Moreover, at the top (reverse) surface  $(y = H)$ , the heat-transfer rate is negligible. For simplicity, a zero-heat-flux condition is imposed on the solid surfaces surrounded by air boundaries. At the left boundary  $(x = 0)$ , the temperature of the solid is maintained at  $T_0$ . Lastly, a zero-gradient condition is employed at the right boundary  $x = L$ .

The heat conduction equation in the coordinate system of  $(x, y)$  is

$$\frac{\partial T}{\partial t} = a \left( \frac{\partial^2 T}{\partial x^2} + \frac{\partial^2 T}{\partial y^2} \right), \quad (1)$$

where  $T$  and  $a$  represent the local temperature of the solid and thermal diffusivity, respectively. The

heat-conduction equation in the  $(\xi, \eta)$  coordinate system is

$$\frac{\partial T}{\partial t} + V_s \frac{\partial T}{\partial \xi} = a \left( \frac{\partial^2 T}{\partial \xi^2} + \frac{\partial^2 T}{\partial \eta^2} \right). \quad (2)$$

Equation (2) is obtained by simple coordinate conversion using the relationships,  $x = \xi + tV_s$  and  $y = \eta$ .

In this study, the inverse-solution method for evaluating the surface heat flux was developed (discussed later). It was validated by using the exact solution of the heat-conduction equation (Eq. 1)

under the aforementioned initial and boundary conditions. To obtain the exact solution in the form of

functions, the surface heat-flux distribution on the cooled side was assumed to be

$$q = -\kappa \left. \frac{\partial T}{\partial y} \right|_{y=0} = \begin{cases} \left( \frac{\kappa A}{2} \right) (\sin\{b_1(x - c_1 + V_s t)\} + 1), & x_1 - V_s t \leq x \leq x_2 - V_s t \\ \left( \kappa A / 2 \right) (\sin\{b_2(x - c_2 + V_s t)\} + 1), & x_2 - V_s t \leq x \leq x_3 - V_s t \\ 0, & \text{otherwise} \end{cases}, \quad (3)$$

where  $\kappa$  denotes the thermal conductivity of the solid; and  $A$ ,  $x_1$ ,  $x_2$ , and  $x_3$  are constants. The location

showing the peak heat flux ( $\kappa A$ ) is a function of time, given as  $x_2 - V_s t$ . The width of the jet-impact

region is given by  $x_3 - x_1$ . During the analysis, we assumed that the high heat-flux region did not reach

the plate edges. In addition, constants  $b_1$ ,  $b_2$ ,  $c_1$ , and  $c_2$  were determined using

$$b_1 = \frac{\pi}{x_2 - x_1}, b_2 = \frac{\pi}{x_3 - x_2}, c_1 = x_1 + \frac{\pi}{2b_1}, c_2 = x_2 - \frac{\pi}{2b_2}. \quad (4)$$

The exact solution can be obtained using a standard technique used for solving partial differential equations, such as the separation-of-variables approach. Because the full derivation of the exact solution requires many pages, only the result is presented. It is expressed as

$$T(x, y, t) = s_1(x, y, t) + s_2(x, y, t) + v_1(x, y, t) + v_2(x, y, t) + T_0, \quad (5)$$

where

$$s_l(x, y, t) = \sum_{k=1} E_k(t) \cdot \sin(\phi_k x) \cdot \frac{\cos h(\phi_k(H-y))}{\phi_k \sin h(\phi_k x)}, \quad \phi_k = \frac{2\pi}{L}(2k-1),$$

and

$$v_l(x, y, t) = \sum_{m=1} \sum_{n=0} (\psi_{mn} u_{mn} + C_{mn}) \exp(-\lambda_{mn} t) \cdot \sin(\mu_m x) \cdot \cos(v_n y),$$

$$\mu_m = \frac{2\pi}{L}(2m-1), v_n = \frac{\pi}{H}n, \lambda_{mn} = a(\mu_m^2 + v_n^2).$$

Here

$$E_k(t) = -\frac{4A}{L\omega_k} \sin\{\mu_k(x_0 - V_s t)\} \cdot \sin\left(\frac{\mu_k \delta}{2}\right) + \frac{A}{L} \left[ \frac{\sin(d_k^+ x + \beta)}{d_k^+} - \frac{\sin(d_k^- x + \beta)}{d_k^-} \right]_{x^- - V_s t}^{x^+ - V_s t};$$

$$\psi_{mn} = \frac{4AV_s}{L} \sin\left(\frac{\mu_m \delta}{2}\right) \left[ \frac{\exp(\lambda_{mn} t)}{\lambda_{mn}^2 + (\mu_m V_s)^2} \{ \lambda_{mn} \cos(\mu_m(x_0 - V_s t)) - \mu_m V_s \sin(\mu_m(x_0 - V_s t)) \} \right]_0^t$$

$$- \frac{2A}{L} \left[ \frac{r_m^+}{d_m^+} \sin(h_m^+) \frac{\exp(\lambda_{mn} t)}{\lambda_{mn}^2 + (r_m^+)^2} \{ \lambda_{mn} \sin(r_m^+ t + g_m^+) - r_m^+ \cos(r_m^+ t + g_m^+) \} \right]$$

$$- \frac{r_m^-}{d_m^-} \sin(h_m^-) \frac{\exp(\lambda_{mn} t)}{\lambda_{mn}^2 + (r_m^-)^2} \{ \lambda_{mn} \sin(r_m^- t + g_m^-) - r_m^- \cos(r_m^- t + g_m^-) \} \Big]_0^t;$$

and

$$u_{mn} = \begin{cases} -\frac{1}{H\mu_m^2}, & n = 0 \\ -\frac{2}{H(\mu_m^2 + v_n^2)}, & n \geq 1 \end{cases} \quad \text{and} \quad C_{mn} = \begin{cases} -\frac{E_m(0)}{H\mu_m^2}, & n = 0 \\ -\frac{2E_m(0)}{H(\mu_m^2 + v_n^2)}, & n \geq 1 \end{cases}.$$

Here,

$$x_0 = \frac{x^+ + x^-}{2}, \quad \delta = x^+ - x^-, \quad \beta = b(-c + V_s t), \quad (x^-, x^+, b, c) = \begin{cases} (x_1, x_2, b_1, c_1), & l = 1 \\ (x_2, x_3, b_2, c_2), & l = 2 \end{cases}$$

$$d_i^+ = b + \mu_i, \quad d_i^- = b - \mu_i, \quad r_i^+ = -\mu_i V_s, \quad r_i^- = \mu_i V_s,$$

$$g_i^+ = d_i^+ \left( \frac{x^+ + x^-}{2} \right) - bc, \quad g_i^- = d_i^- \left( \frac{x^+ + x^-}{2} \right) - bc, \quad h_i^+ = d_i^+ \left( \frac{x^+ - x^-}{2} \right), \quad h_i^- = d_i^- \left( \frac{x^+ - x^-}{2} \right),$$

in which  $d_i$  is assumed to be non-zero.

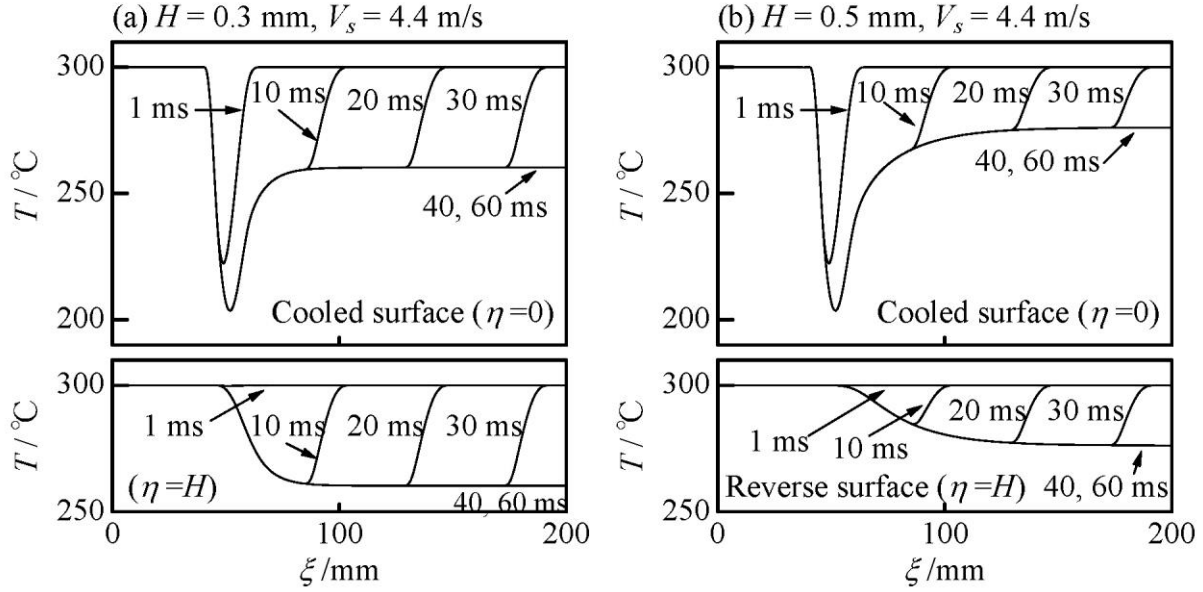
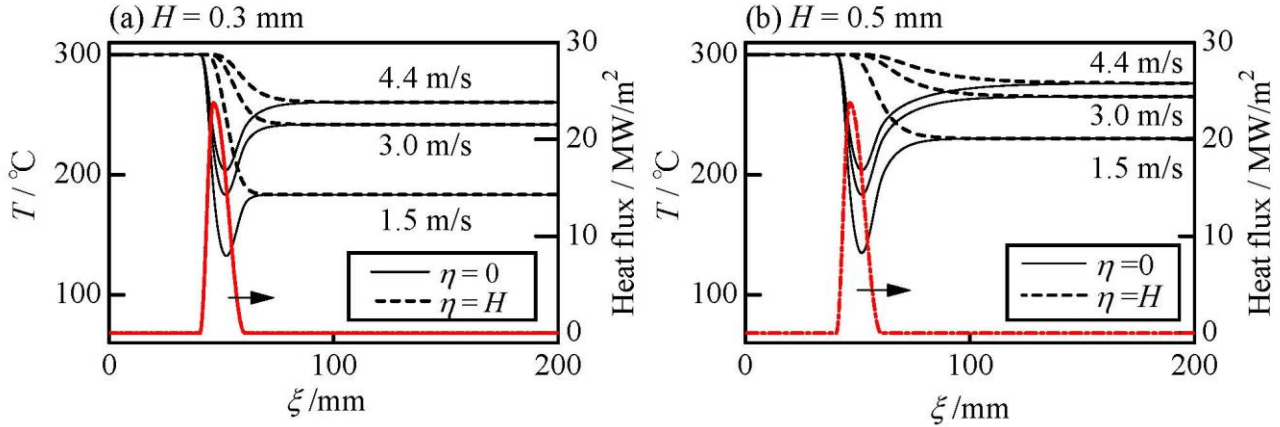


**Figure 3** Examples of transient temperature profiles inside the cooled and reverse surfaces, calculated using the exact solution of Eq. 5 for:  $V_s = 4.4$  m/s,  $t = 0\text{--}60$  ms, and  $H =$  (a) 0.3 and (b) 0.5 mm

Figure 3 presents the examples of the time history of temperature profiles on the cooled and reverse surfaces. They were calculated using the exact solution under the conditions that the plate thickness  $H = 0.3$  and 0.5 mm, velocity of the solid  $V_s = 4.4$  m/s, initial temperature of the solid  $T_0 = 300$  °C, thermal diffusivity  $a = 5.25 \times 10^{-6}$  m/s<sup>2</sup>, width of jet-impact region  $x_3 - x_1 = 20$  mm ( $x_2 - x_1 = 6$  mm, and  $x_3 - x_2 = 14$  mm ( $x_2 = 46$  mm)), plate length  $L = 1$  m, and peak value of the heat flux in the jet-impact region  $(\kappa A) = 23.8$  MW/(m·K). Note that these numerical conditions except for the plate length were set considering laboratory-scale experiments, which are discussed later. The results are presented in the  $\xi$ -coordinate system. We observed that both temperatures on the cooled and reverse surfaces varied with

time and shortly reached a quasi-steady state. The results suggested that analysis was possible at that state in the  $(\xi, \eta)$  coordinate system, using the heat-conduction equation

$$V_s \frac{\partial T}{\partial \xi} = a \left( \frac{\partial^2 T}{\partial \xi^2} + \frac{\partial^2 T}{\partial \eta^2} \right). \quad (6)$$



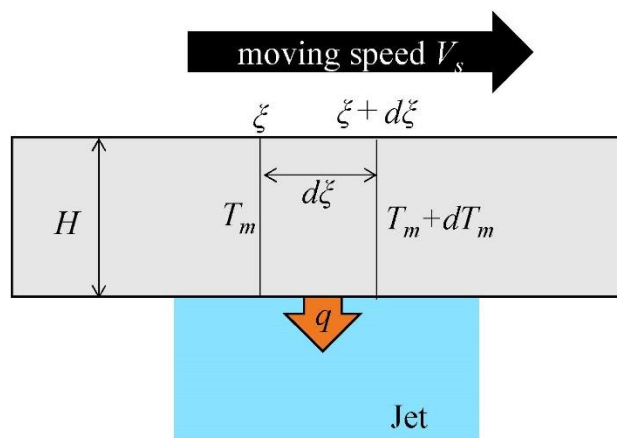
**Figure 4** Exact solutions for varying velocity of solid ( $V_s = 1.5, 3.0,$  and  $4.4$  m/s) and  $H =$  (a)  $0.3$ ; and (b)  $0.5$  mm

Figure 4 shows the temperature profiles on both the cooled and reverse surfaces in a quasi-steady state obtained by varying the velocity of the solid as a parameter. The imposed heat flux on the cooled surface is also presented in Figure 4. The other numerical conditions are the same as those in Fig. 3. On the cooled surface, the temperature was maintained at the initial value, upstream of the jet impingement, and decreased sharply in the jet-impact region, followed by some heat recovery. Moreover, the temperature remained constant in the downstream region. On the reverse side, the temperature variation was small compared to that of the cooled surface, and there was no heat recovery.

As expected, the temperature variation on the reverse side was small for thick solids. In the downstream region, where the temperatures on the cooled and reverse surfaces matched, the solid is isothermal. Furthermore, the temperature profile was influenced by the velocity of the solid. These results were used to validate the developed evaluation methods. Note that the exact solution (Eq. 5) includes some infinite series. The calculations were conducted up to  $m = 30000$  and  $n = k = 300$  to obtain smooth temperature profiles. The temperature profiles were smooth up to approximately 7 decimal places.

### 3. Evaluation methods for surface heat flux on the cooled surface

In this study, we developed two types of models capable of evaluating the surface heat flux: a simple model and an IHCP-based model.



**Figure 5** Schematic of the simple model

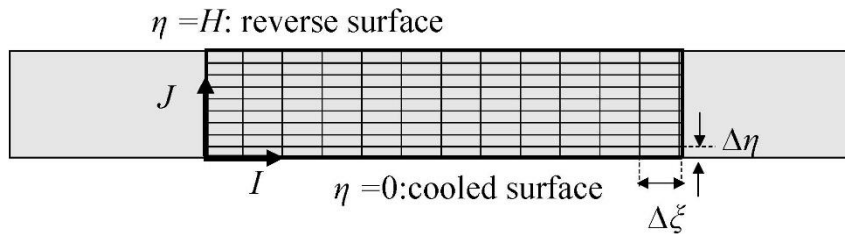
#### 3.1 Simple model

Figure 5 shows a schematic of the simple model used to evaluate the heat-transfer rate on the cooled surface. The model is based on energy conservation for a control volume defined by the two boundaries

at  $\zeta = \zeta$  and  $\zeta + d\zeta$ . We assume that heat removal from the solid surface on the cooled side corresponds to a change in the internal energy of the solid. At the upstream boundary, the heat of  $\rho c V_s H T_m$  enters the control volume per unit time, where  $T_m$  is the local temperature of the solid, averaged in the thickness direction. Moreover,  $\rho$  and  $c$  are the material density and specific heat, respectively. At the downstream boundary, heat exits with value  $\rho c V_s H (T_m + dT_m)$ . The heat removal rate on the cooled side is denoted by  $q d\zeta$ , where  $q$  is the local heat flux passing through the cooled surface. Assuming that heat conduction in the  $\zeta$ -direction and heat removal on the reverse side are negligibly small compared to the heat removal on the cooled surface, a simple application of the energy-conservation law yields the equation

$$q = \rho c V_s H \frac{dT_m}{d\zeta}. \quad (7)$$

In this model, the measured surface temperature,  $T_{surf}$ , is used as the value of  $T_m$  because  $T_m$  cannot be correctly determined. Note that the simple model corresponds to ‘lumped capacitance model’ of a small control volume in coordinates  $(x, y)$  [12,23].



**Figure 6** Overview of computational domain

### 3.2 Model based on the steady-state heat conduction equation

This model is based on the steady-state heat-conduction equation (Eq. 6) in the  $(\zeta, \eta)$  coordinate system. The equation is numerically solved using the finite difference technique [24]. Figure 6 shows a schematic of the analytical rectangular domain, divided into multiple rectangular cells with dimensions  $\Delta\zeta$  and  $\Delta\eta$ . In the analysis, the cell size  $\Delta\zeta$  corresponds to the pixel size of the infrared camera. Because the plate is thin, we assume  $\Delta\zeta \gg \Delta\eta$ . Each cell is numbered with the subscripts  $I$  ( $I = 1, 2, \dots, N$ ) and  $J$  ( $J = 1, 2, \dots, M$ ) in the  $\zeta$  and  $\eta$ -directions, respectively. Each term of Eq. (6) is approximated using the following finite-difference schemes:

$$V_s \frac{\partial T}{\partial \zeta} = V_s \frac{T_{I-2,J} + (2\varepsilon - 6)T_{I-1,J} + (3\varepsilon + 1)T_{I,J} + (2 - 6\varepsilon)T_{I+1,J} + \varepsilon T_{I+2,J}}{6(1 - \varepsilon)\Delta\zeta} + O((\Delta\zeta)^3); \quad (8)$$

$$\frac{\partial^2 T}{\partial \zeta^2} = \frac{-T_{I-2,J} + 16T_{I-1,J} - 30T_{I,J} + 16T_{I+1,J} - T_{I+2,J}}{12(\Delta\zeta)^2} + O((\Delta\zeta)^4); \quad (9)$$

and

$$\frac{\partial^2 T}{\partial \eta^2} = \frac{T_{I,J-1} - 2T_{I,J} + T_{I,J+1}}{(\Delta\eta)^2} + O((\Delta\eta)^2). \quad (10)$$

Note that the scheme adopted in the  $\zeta$ -direction has higher order than that in the  $\eta$ -direction, considering  $\Delta\zeta \gg \Delta\eta$ . Additionally,  $\varepsilon$  in Eq. (8) is the control parameter. For  $\varepsilon = 0$  and  $V_s > 0$ , the scheme is upwind (UTOPIA scheme) [25]. Moreover,  $\varepsilon \rightarrow \infty$  corresponds to the UTOPIA scheme in the reverse direction. For reference, the scheme is called ‘downwind scheme’ in the present study. Furthermore, if  $\varepsilon = -1$ , it becomes a fourth-order central difference scheme.

The present model is based on previous studies [21, 22]. The third-order upwind scheme was adopted in the first derivative term and the second-order central difference scheme was employed in the second derivative term in the  $\zeta$ -direction. The main difference between the present model and those of the earlier studies is the control parameter  $\varepsilon$  in Eq. (8). As will be shown later, it significantly influences the evaluated surface heat flux.

Substituting Eqs. (8–10) into Eq. (6), we obtain the approximated equation

$$T_{I,J-1} = \frac{V_s(\Delta\eta)^2}{6a(1-\varepsilon)\Delta\xi} (T_{I-2,J} + (2\varepsilon - 6)T_{I-1,J} + 3(\varepsilon + 1)T_{I,J} + (2 - 6\varepsilon)T_{I+1,J} + \varepsilon T_{I+2,J}) + \frac{(\Delta\eta)^2}{12(\Delta\xi)^2} (-T_{I-2,J} + 16T_{I-1,J} - 30T_{I,J} + 16T_{I+1,J} - T_{I+2,J}) - (2T_{I,J} - T_{I,J+1}). \quad (11)$$

For the numerical procedure,  $T_{surf}$  is known at the reverse surface ( $\eta = H$ ). Moreover, a relationship is established as

$$q_{reverse\_surface} = h\Delta T = -\kappa \left. \frac{\partial T}{\partial \eta} \right|_{reverse\_surface}, \quad (12)$$

where  $q_{reverse\_surface}$ ,  $h$ , and  $\Delta T$  are the local surface heat flux, heat-transfer rate, and temperature difference between the solid and ambient air, respectively. Note that, for simplicity, the exact solution is obtained by assuming zero surface-heat-flux on the reverse side. By applying the first-order finite difference approximation to Eq. (12), the temperature at a small distance from the reverse surface can be calculated. Thereafter, the local temperature  $T_{I,J}$  is calculated using Eq. (11) for the cooled surface ( $\eta = 0$ ).

In the present analysis, the cell size  $\Delta\xi$  was set to 0.5 mm, considering the resolution of the infrared camera used in the conducted experiments. The cell size ( $\Delta\eta = 0.0015$  mm) in the  $\eta$ -direction was determined by conducting several preliminary grid-convergence tests.

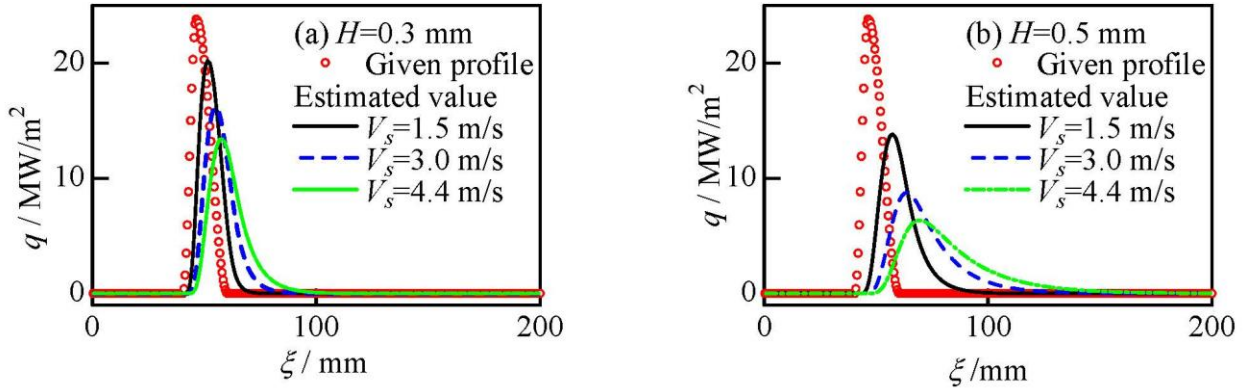
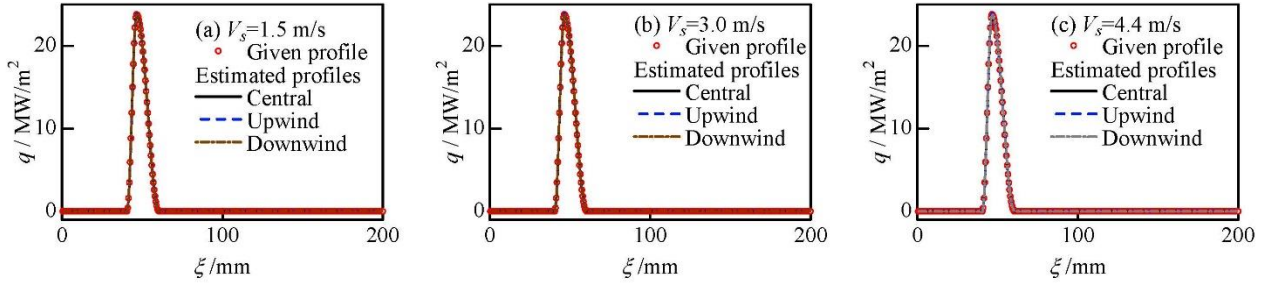


**Figure 7** Validations of simple model by comparing the predictions with the given profile for:  $H =$  (a) 0.3 and (b) 0.5 mm;  $V_s = 1.5, 3.0,$  and  $4.4$  m/s

### 3.3 Model validation

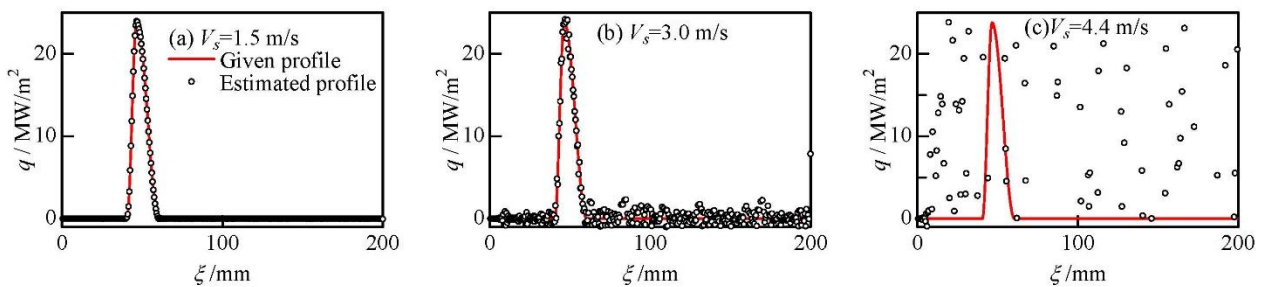
Figure 7 depicts a comparison of the heat-flux profiles given by Eq. (3), with the predicted values obtained using the simple model.  $dT_m/d\xi$  in Eq. (7) was evaluated using the exact solution at the reverse surface. The model predictions agree reasonably well with the given conditions for  $H = 0.3$  mm and  $V_s = 1.5$  m/s. However, appreciable deviations were observed in other cases. The predicted peak heat flux is significantly smaller than the given heat-flux profiles, particularly for the thick plates with higher velocities. Additionally, with velocity increase, the peak shifts downstream, and the band

showing relatively large heat flux grows. We concluded that the simple model is unsuitable for evaluating the heat-flux distributions in the jet-impact region.



**Figure 8** Comparisons of the given heat flux with model predictions for  $H = 0.3$  mm and  $V_s =$  (a) 1.5, (b) 3.0, and (c) 4.4 m/s

Next, IHCP-based model was validated. Figure 8 displays a comparison of the given and estimated results of the cooled surface for  $H = 0.3$  mm. The velocity of the solid was varied ( $V_s = 1.5, 3.0,$  and  $4.4$  m/s). Additionally, the parameter  $\varepsilon$  in Eq. (8) was varied as  $\varepsilon = -1, 0,$  and  $\infty$ . For all cases, the model predictions were in good agreement with the given profiles, suggesting that the developed model can correctly evaluate the heat-transfer characteristics. In this case, the predictions were independent of  $\varepsilon$ .



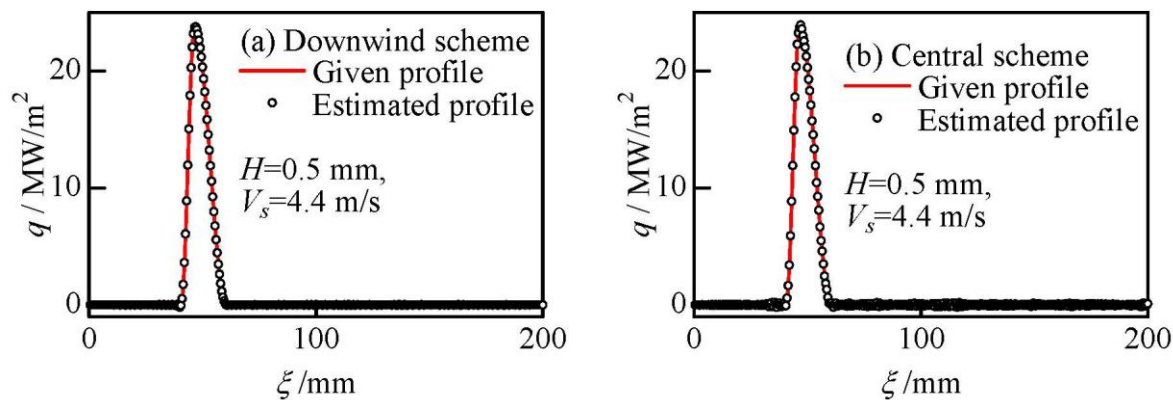
**Figure 9** Comparisons of the given heat flux and model predictions when  $\varepsilon = 0$  (upwind scheme) for  $H = 0.5$  mm and  $V_s =$  (a) 1.5, (b) 3.0, and (c) 4.4 m/s.

Figure 9 displays the estimated and given heat-flux profiles on the cooled surface for  $H = 0.5$  mm. The result for  $V_s = 1.5$  m/s agrees reasonably well with the given profile. In the case of  $V_s = 3.0$  m/s, small fluctuations appear. For  $V_s = 4.4$  m/s, the model prediction shows unrealistic fluctuations in the entire region, implying failure of the inverse analysis. The results imply that the evaluation model in [21, 22] is inapplicable to the present case.

We conducted multiple numerical tests under various conditions and observed that such unrealistic numerical fluctuations occurred for large velocities and thick solids. First, the reason for the errors in the case of a thick solid was examined. In the model, the calculation proceeds in the direction opposite to the path along which the cooling propagates. In other words, the calculation is solving for negative thermal-diffusion phenomenon. Any small-scale errors occurring at or near the reverse surface were amplified by departure. Consequently, the magnitude of the amplified errors was large for thick solids. Second, we discuss the reason for errors in the case of large velocities. There was no error on the reverse side because the temperature was given by the exact solution. Judging from the fact that the errors were appreciable for a large velocity of the solid, the main error source was the finite-difference approximation of the term including the solid's velocity. We conducted many simulations varying the

parameter  $\varepsilon$ , and observed that unrealistic fluctuations were partially suppressed by using the downwind or central-difference schemes. Figure 10 shows the results estimated by these schemes under the conditions  $H = 0.5$  mm and  $V_s = 4.4$  m/s. The numerical errors were significantly reduced and the downwind scheme was a better choice than the upwind scheme. The upwind scheme is inadequate because the inverse analysis proceeds backwards toward the actual heat-transport path.

In the numerical analysis of the transient transport equation, the central-difference scheme is commonly employed for the diffusion terms, but it is not applied to the first derivative term. Consequently, we used downwind scheme for the first derivative term of temperature in the present model.



**Figure 10** Comparison of the given heat flux and model predictions for  $H = 0.5$  mm and  $V_s = 4.4$  m/s, when (a)  $\varepsilon = \infty$  and (b)  $\varepsilon = -1$

### 3.4 Smoothing operation of temperature profiles on the reverse side

In Subsection 3.3, we observed that small errors due to the finite-difference approximation condition induced unrealistic numerical fluctuations. In this subsection, we focus on errors associated with the temperature profile on the reverse side.

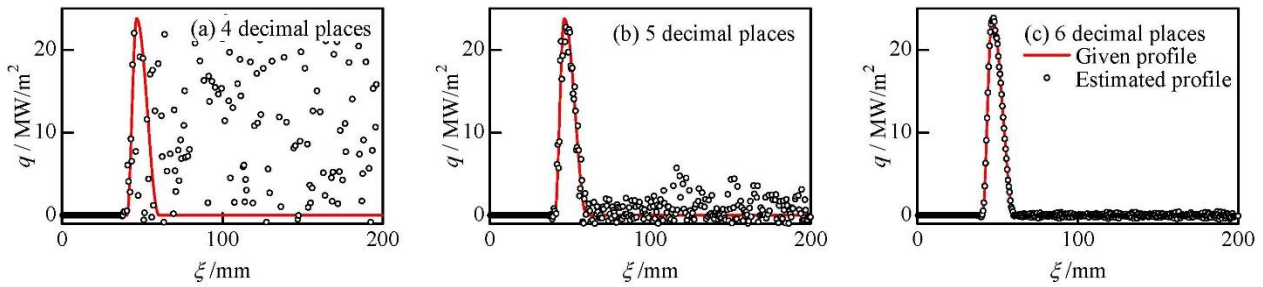


**Figure 11** Heat-flux profiles on the cooled surface evaluated using the temperature rounded off from the exact solution to 4–6 decimal places for the case of  $H = 0.5$  mm and  $V_s = 4.4$  m/s

Figure 11 shows the evaluated heat flux profiles on the cooled surface for the case of  $V_s = 4.4$  m/s and  $H = 0.5$  mm obtained using the temperature profile on the reverse side. It is calculated by rounding the exact solution off to 4–6 decimal places. For example, in the case of 4 decimal places, the value of 289.6688632... is rounded to 289.6689. Although the deviation of the tested temperature profile from the exact solution is considerably small, unrealistic fluctuations appear for the cases of 4 and 5 decimal places. The fluctuations are caused by numerical errors in the finite-difference approximation to the first derivative term in Eq. (8). The present model is highly sensitive to small errors in the temperature

profile on the reverse surface. In addition, we conducted many numerical tests and found that unrealistic fluctuations are more appreciable when smaller cell size,  $\Delta\xi$ , is employed.

Next, we artificially created temperature profiles  $Y$  on the reverse side by adding a random error ( $\omega$ ) to the exact solution ( $T_{exact}$ ) as  $Y = T_{exact} + \omega$ . The random error is given by zero-mean noise with a Gaussian distribution [26, 27]. The standard deviation of the noise was set to 0.83, corresponding to  $|\omega| < 2.5$  °C. Figure 12(a) displays the artificial temperature profile,  $Y$ , on the reverse surface ( $\eta = H$ ) for  $H = 0.5$  mm and  $V_s = 4.4$  m/s. As expected, the inverse analysis using the temperature profile failed. These results indicate the need for the profile's data smoothing or noise reduction in advance.

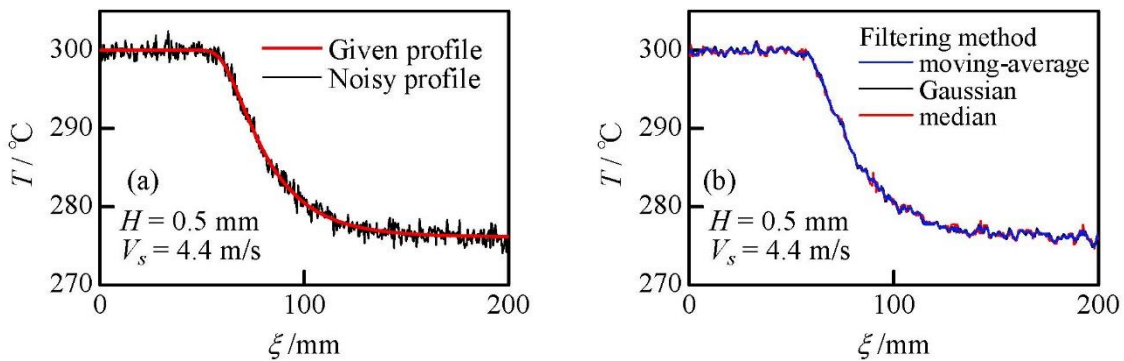


**Figure 12** (a) Artificial temperature profile,  $Y$ , on the reverse surface for  $H = 0.5$  mm and  $V_s = 4.4$  m/s, and (b) temperature profiles obtained using various digital filtering methods.

In this study, we tested two types of noise-reduction techniques. The first involved digital filtering, including moving-average [28], Gaussian [29], and median filters [30]. However, the approach was unsuccessful. Figure 12(b) shows some filtered temperature profiles, which are noisy. The other

technique involved building a smooth fitting function for the noisy-temperature profile using the least-squares technique. We first attempted to use a single polynomial function, but it was also unsuccessful. Subsequently, a spline function consisting of multiple piecewise polynomial functions was tested. Figure 13(a) shows an example of the smoothed temperature profile to noisy ones using a linear combination of 8<sup>th</sup>-order B-splines, computed with the de Boor algorithm [31]. The number of spline functions was 33. The B-splines for smoothing data with noise reduction showed the best fit to the given temperature profile in the jet-impact region. However, some errors remained in the upstream and downstream regions, where the magnitude of noise is appreciably larger than the true temperature variation, and induced unrealistic fluctuations. We found that using low order B-splines can reduce the fluctuations in such regions. Therefore, we introduced additional constraint conditions,  $d^3S(\zeta)/d\zeta^3 = 0$ , in the upstream and downstream regions away from the jet-impact region, where  $S(\zeta)$  is the spline function fitting the noisy profile. The constraint conditions imply the order of B-splines is partially reduced. Note that the constraint conditions were applicable only to the current case, where the outline of the temperature profile was known. The results for the constraint conditions are shown in Fig. 13(b). The smoothed curve significantly matches the given temperature profile, and no fluctuation is observed in the upstream and downstream regions.

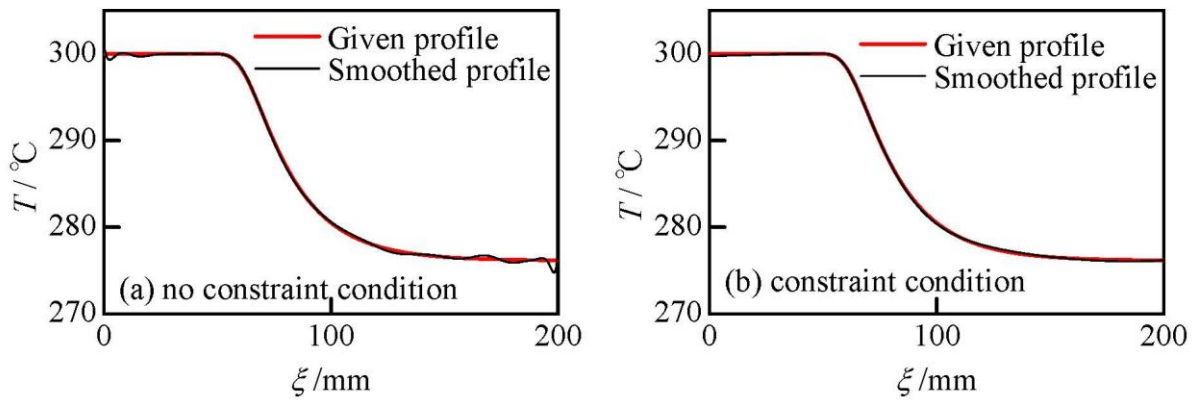


**Figure 13** Comparison of the given temperature profile (exact solution) after smoothing with the noisy profile: (a) without and (b) with constraint conditions

Figure 14 displays the evaluated heat-flux profiles on the cooled surface ( $\eta = 0$ ), using the smoothed temperature profile shown in Fig. 13(b). Although a small error remained, the evaluated heat flux reasonably agreed with the given profile. In addition, due to high dependency on the smoothing operation, conducting uncertainty analysis was difficult using this model. As indicated by the results, the uncertainty of the evaluated heat flux was a few  $\text{MW/m}^2$ .

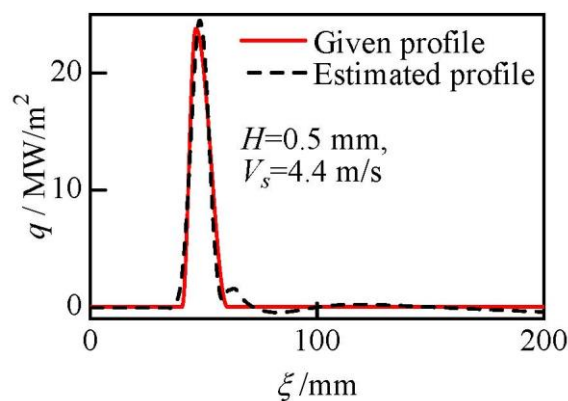


**Figure 14** Estimated temperature and heat flux of the cooled surface ( $\eta = 0$ ), from smoothed temperature profiles of the uncooled surface ( $\eta = H$ ) given in Fig. 13(b)

#### 4. Model extension to three dimensions and application to laboratory-scale experiments

A 3-D model for evaluating the surface was easily obtained by adding a coordinate axis to the 2-D model. The heat-conduction equation in a 3-D system, fixed in space, is given by

$$V_s \frac{\partial T}{\partial \xi} = a \left( \frac{\partial^2 T}{\partial \xi^2} + \frac{\partial^2 T}{\partial \eta^2} + \frac{\partial^2 T}{\partial \zeta^2} \right), \quad (13)$$

where  $\zeta$  is the width of the solid. The corresponding finite-difference scheme is given by

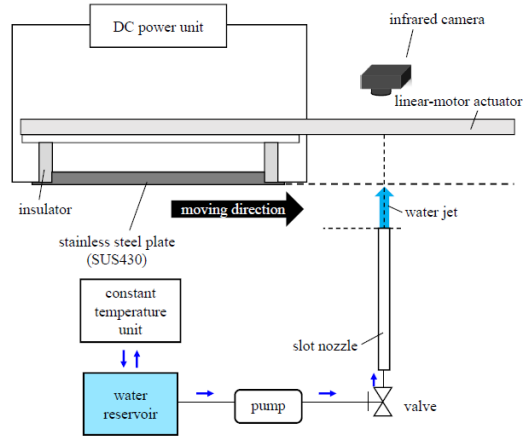
$$\begin{aligned} & T_{I,J-1,K} \\ &= \frac{V_s(\Delta\eta)^2}{6a(1-\varepsilon)\Delta\xi} (T_{I-2,J,K} + (2\varepsilon - 6)T_{I-1,J,K} + 3(\varepsilon + 1)T_{I,J,K} + (2 - 6\varepsilon)T_{I+1,J,K} + \varepsilon T_{I+2,J,K}) \\ &+ \frac{(\Delta\eta)^2}{12(\Delta\xi)^2} (-T_{I-2,J,K} + 16T_{I-1,J,K} - 30T_{I,J,K} + 16T_{I+1,J,K} - T_{I+2,J,K}) \\ &+ \frac{(\Delta\eta)^2}{12(\Delta\zeta)^2} (-T_{I,J,K-2} + 16T_{I,J,K-1} - 30T_{I,J,K} + 16T_{I,J,K+1} - T_{I,J,K+2}) - (2T_{I,J,K} - T_{I,J+1,K}). \end{aligned} \quad (14)$$

Next, the smoothing operation using the 8th-order B-spline functions in 2-D was performed, with the following constraint conditions:  $\partial^3 S(\xi, \zeta) / \partial \xi^3 = \partial^3 S(\xi, \zeta) / \partial \zeta^3 = 0$ , in the upstream region, where the temperature is almost constant. Moreover, no constraint conditions were adopted in the downstream region because the ‘‘correct temperature profile’’ was unknown in the experiments.

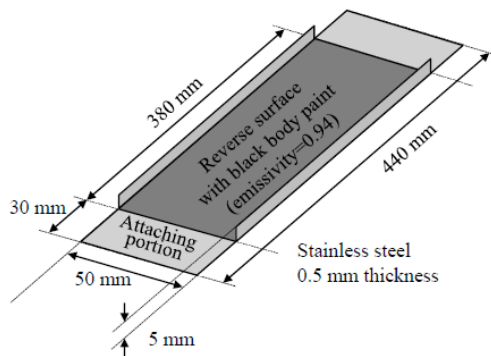
In addition, the temperature dependence on metal plate properties such as density, specific heat, and thermal conductivity were considered. The heat-transfer coefficient ( $h$ ), between the ambient air and the reverse-side solid surface, was set to  $250 \text{ W}/(\text{m}^2 \text{ K})$  [23].

Figure 15(a) shows a schematic of the experimental apparatus used to study the heat-transfer characteristics in planar water-jet cooling of a hot, moving metal sheet. The apparatus was composed of: (1) a water-supply system to create a vertically-upward planar jet, (2) linear-motor actuator for moving the hot test sheet, (3) observation equipment, and (4) DC power supply for electrically heating the sheet.

Water at  $17 \text{ }^\circ\text{C}$  was used as the test coolant. It was stored in a reservoir tank equipped with a constant temperature unit (ASONE, Carry Cool 301CN) and transported by a mechanical pump to a slot nozzle through a regulating valve. An upward planar jet was emitted from the mouth of the vertical slot-nozzle with a cross-section of  $1.1 \text{ mm} \times 66.0 \text{ mm}$ . The water-flow rate  $Q$  was determined by measuring the discharged volume for a sampling time of 30 s. The rate was fixed to  $6.35 \text{ L}/\text{min}$ .



(a) setup



(b) test sheet

**Figure 15** (a) Schematic of experimental apparatus and (b) dimensions of test plate

Fig. 15(b) shows the dimensions of the test sheet made of stainless steel (SUS430). The arithmetic-mean surface roughness,  $R_a$ , of the test sheet was within  $0.2 \mu\text{m}$ . The longer sides of the sheet were bent at right angles, 5 mm from the edges, to reduce unwanted buckling from thermal stress during the cooling tests. The test sheet was also pulled in the longitudinal direction with approximately 150 N.

Further, a thin coat of black-body paint with emissivity of 0.94 was added to the reverse of the jet-impact surface for maximum accuracy in infrared-camera measurements.

The test sheet was mounted on a linear motor with a stroke of 2500 mm (FESTO, ELGA-TB-RF). Initially, the test sheet was heated to a preset temperature (200–600 °C) using a DC power supply with a peak output of 5 kW (TEXIO, PU10-500). Then, the test sheet was steeply accelerated at  $15 \text{ m/s}^2$ , reaching a preset velocity (1.5, 3.0, or 4.4 m/s), entered the cooling section, and decelerated at  $-15 \text{ m/s}^2$  to zero velocity at the other end. An infrared camera (Nippon AVIONICS, U100SP) with a resolution of  $320 \times 240$  pixels at 60 frames per second was set approximately 300 mm away from the test sheet, and it captured the surface-temperature profile on the reverse side. The measurement accuracy was within  $\pm 2\%$  to the measured value (specified by the manufacturer). The actual length captured by one pixel of the camera sensor corresponds to 0.57 mm. Notably, the length of the test sheet was selected considering the time required to reach a quasi-steady state, as shown in Figure 3. The temperature-measurement phase was conducted after the time it took to capture the quasi-steady state temperature profile. The temperature measurement was conducted under the dark-room conditions to omit unwanted infrared light.

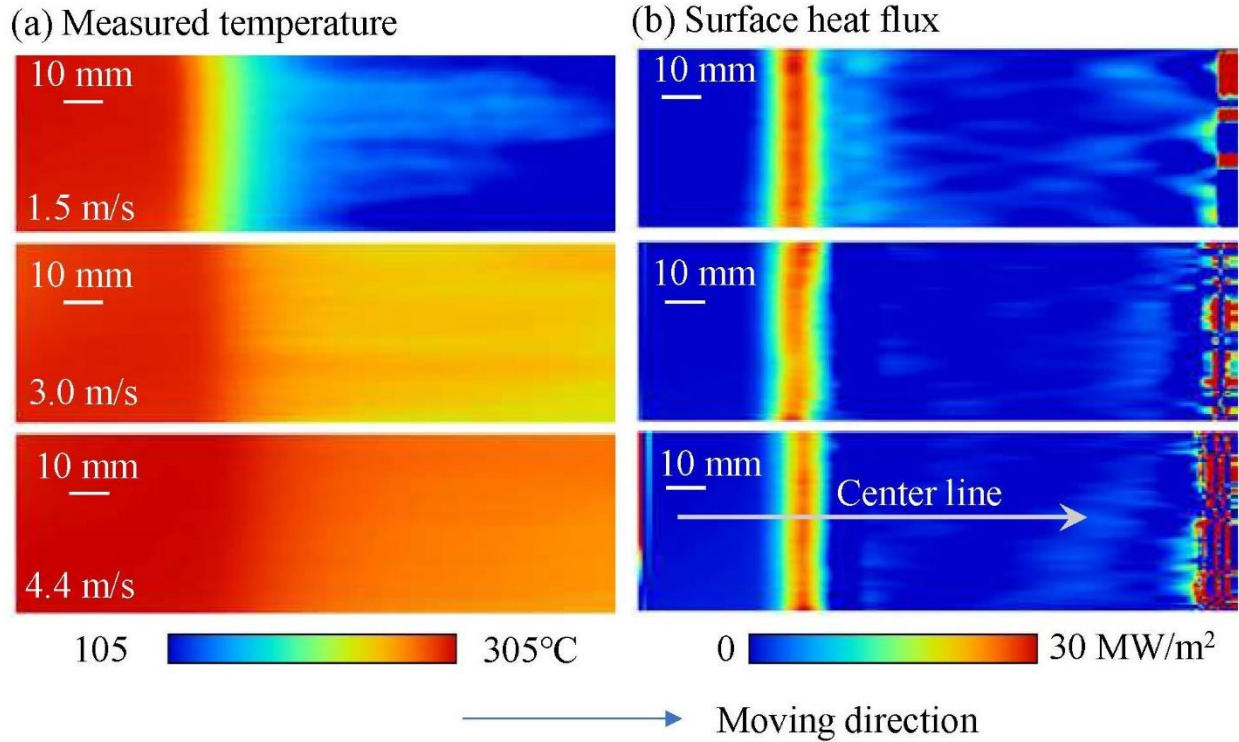


**Figure 16** Temperature profile of (a) the uncooled surface and (b) estimated heat flux distribution for  $T_0 = 300\text{ }^\circ\text{C}$ ,  $H = 0.5\text{ mm}$ , and  $Q = 6.35\text{ L/min}$ .

Figure 16 depicts (a) the measured temperature profile on the reverse surface (without smoothing operation) and (b) the surface heat-flux distribution evaluated using the smoothed temperature profile under the conditions that the water flow rate was 6.35 L/min, initial temperature of the solid was 300 °C, and moving velocities of the test plate were 1.5, 3.0, and 4.4 m/s. As expected, the temperature drop was larger for smaller velocities of the solid plate, as the local contact time of coolant to the moving solid was longer. The temperature variation was expectedly small on the reverse surface and large on the cooled surface. Linear high heat-flux regions, in the width dimension, appeared in all cases. This suggests that planar jet-impingement can achieve uniform cooling along the jet line. In addition,

intensive cooling was achieved only in the jet-impact zone, unlike the results evaluated using the simple model shown in Figure 7. The current 3-D model adequately evaluates the surface heat flux as well as the temperature distribution in the jet-impact region.

Incidentally, there were apparently unrealistic fluctuations near the downstream boundaries because no constraint conditions were imposed in the downstream region in the inverse analysis. Therefore, further progress in the 3-D model is a prospect for future studies.

To investigate the heat-transfer characteristics in the jet-impact region, we introduced an index called “maximum heat flux,” defined as the highest heat-flux value along the center line of the moving solid. The centerline is shown in Fig. 16. The point showing maximum heat flux is present near a place where the cooling water is in first contact with a dry moving solid; thus, the value is considerably high. Figure 17 shows the maximum heat flux under varying temperature and velocity of the solid. Note that the experiments were conducted five times for each condition to ensure reproducibility, and the mean values are plotted in the figure 17. The error bars represent the standard deviation of experimental data. The result for  $T_0 = 300\text{ }^\circ\text{C}$  and  $V_s = 1.5\text{ m/s}$  is missing because the unwanted buckling of solid occurs during the cooling. The maximum heat flux increases with the increase in the initial temperature of the solid, attains a maximum value, decreases, reaches a minimum, and increases again. The transition boiling occurs in the temperature range between the local peak and valley values, and the film boiling

occurs in the range higher than the valley. Similar results were obtained in references [21, 22] studying the circular jet impingement on a dry, moving solid. The boundaries of nucleate-to-transition boiling, and transition-to-film boiling are present at higher temperatures for smaller moving velocities. The results can be expressed by the contact time of water jet with local solid, as shown in Figure 16. The local-solid temperature in the jet-impact region is lower for a smaller moving velocity.

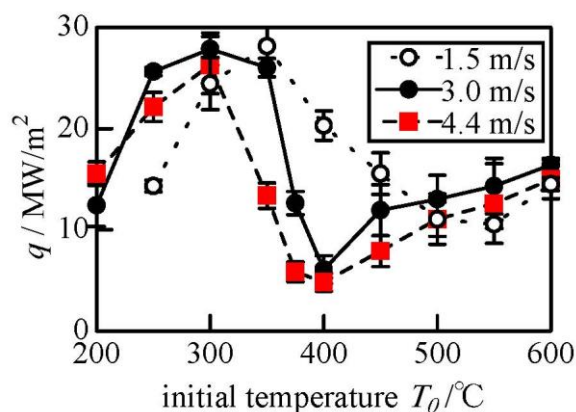


**Figure 17** Maximum heat flux under various conditions for  $H = 0.5$  mm and  $Q = 6.35$  L/min.

## 5. Conclusions

In this study, we developed two models capable of evaluating the surface heat flux in water-jet cooling of a moving hot solid. The models were validated using the exact solutions of the steady-state heat-conduction equation. Additionally, the IHCP-based model was extended to three dimensions. The 3-D model was adopted for the laboratory-scale experiments. The results are summarized as follows:

- (1) The applicability of the simple model was considerably limited. Reasonable predictions were obtained only when the thickness and velocity of the solid were 0.3 mm and 1.5 m/s, respectively.
- (2) The IHCP-based model was highly sensitive to the finite-difference approximation scheme for the first derivative term and small errors on the reverse surface. These conditions caused unrealistic fluctuations in the temperature profile of the cooled surface. The errors were reduced to some extent using the downwind scheme, and the smoothing operation of the measured temperature profile. The B-spline function with constraint boundary conditions proved to be a good choice for the current model.
- (3) The 3-D model was applied to laboratory-scale experiments and proved to be a useful tool for evaluating the surface heat flux. However, further investigation is required to reduce inherent estimation errors. This is a potential avenue for future work.
- (4) The boiling heat transfer is significantly dependent on the temperature of the solid and moving velocity. The effect of varying the velocity can be expressed by the contact time of the jet with the local solid surface.

## **6. Conflict of interest**

The authors declare that they have no known competing financial interests or personal relationships that could have appeared to influence the work reported in this study.

## 7. References

- [1] R. Wu, T. Hong, Q. Cheng, H. Zou, Y. Fan, X. Luo, Thermal modeling and comparative analysis of jet impingement liquid cooling for high power electronics, *Int. J. Heat Mass Transf.* 137 (2019) 42–51. <https://doi.org/10.1016/j.ijheatmasstransfer.2019.03.112>.
- [2] P. Yu, K. Zhu, T. Sun, N. Yuan, J. Ding, Heat transfer rate and uniformity of mist flow jet impingement for glass tempering, *Int. J. Heat Mass Transf.* 115 (2017) 368–378. <http://doi.org/10.1016/j.ijheatmasstransfer.2017.08.065>.
- [3] M. Gradeck, A. Kouachi, M. Lebouché, F. Volle, D. Maillet, J.L. Boreau, Boiling curves in relation to quenching of a high temperature moving surface with liquid jet impingement, *Int. J. Heat Mass Transf.* 52 (2009) 1094–1104. <https://doi.org/10.1016/j.ijheatmasstransfer.2008.09.015>.
- [4] A.T. Hauksson, D. Fraser, V. Prodanovic, I. Samarasekera, Experimental study of boiling heat transfer during subcooled water jet impingement on flat steel surface, *Ironmaking Steelmaking*. 31 (2004) 51–56. <https://doi.org/10.1179/030192304225011098>.

- [5] F. Xu, M.S. Gadala, Heat transfer behavior in the impingement zone under circular water jet, Int. J. Heat Mass Transf. 49 (2006) 3785–3799. <https://doi.org/10.1016/j.ijheatmasstransfer.2006.03.034>.
- [6] M.A. Islam, M. Monde, P.L. Woodfield, Y. Mitsutake, Jet impingement quenching phenomena for hot surfaces well above the limiting temperature for solid–liquid contact, Int. J. Heat Mass Transf. 51 (2008) 1226–1237. <https://doi.org/10.1016/j.ijheatmasstransfer.2007.01.059>.
- [7] G.G. Guedia Guemo, V. Prodanovic, M. Militzer, Modeling of transient bottom jet impingement boiling, Int. J. Heat Mass Transf. 136 (2019) 1160–1170. <https://doi.org/10.1016/j.ijheatmasstransfer.2019.03.060>.
- [8] D. Kashyap, V. Prodanovic, M. Militzer, Transient bottom jet impingement cooling of steel, ISIJ Int. 60 (2020) 1743–1751. <https://doi.org/10.2355/isijinternational.ISIJINT-2019-691>.
- [9] K.V. Jondhale, M.A. Wells, M. Militzer, V. Prodanovic, Heat transfer during multiple jet impingement on the top surface of hot rolled steel strip, Steel Res. Int. 79 (2008) 938–946. <https://doi.org/10.1002/srin.200806224>.
- [10] H. Wang, W. Yu, Q. Cai, Experimental study of heat transfer coefficient on hot steel plate during water jet impingement cooling, J. Mater. Process. Technol. 212 (2012) 1825–1831. <http://doi.org/10.1016/j.jmatprotec.2012.04.008>.

- [11] S. Vakili, M.S. Gadala, Boiling heat transfer of multiple impinging jets on a hot moving plate, Heat Transf. Eng. 34 (2013) 580–595. <https://doi.org/10.1080/01457632.2013.730412>.
- [12] Q. Xie, B. Wang, Z. Wang, G. Wang, Heat transfer coefficient and flow characteristics of hot steel plate cooling by multiple inclined impinging jets, ISIJ Int. 56 (2016) 2236–2242. <http://doi.org/10.2355/isijinternational.ISIJINT-2015-509>.
- [13] M. Gradeck, A. Kouachi, J.L. Borean, P. Gardin, M. Lebouché, Heat Transfer from a hot moving cylinder impinged by a planar subcooled water jet, Int. J. Heat Mass Transf. 54 (2011) 5527–5539. <https://doi.org/10.1016/j.ijheatmasstransfer.2011.07.038>.
- [14] A.K. Mozumder, Y. Mitsutake, M. Monde, Subcooled water jet quenching phenomena for a high temperature rotating cylinder, Int. J. Heat Mass Transf. 68 (2014) 466–478. <http://doi.org/10.1016/j.ijheatmasstransfer.2013.09.059>.
- [15] M. Jahedi, F. Berntsson, J. Wren, B. Moshfegh, Transient inverse heat conduction problem of quenching a hollow cylinder by one row of water jets, Int. J. Heat Mass Transf. 117 (2018) 748–756. <https://doi.org/10.1016/j.ijheatmasstransfer.2017.10.048>.
- [16] J.M. Jha, S.V. Ravikumar, I. Sarkar, S.K. Pal, S. Chakraborty, Jet impingement cooling of a hot moving steel plate: an experimental study, Exp. Heat Transf. 29 (2016) 615–631. <https://doi.org/10.1080/08916152.2015.1046019>.

- [17] N. Nakata, T. Kuroki, A. Fujibayashi, Y. Hino, Y. Utaka, Evaluation of cooling performance in intensive cooling with high water flow rate and effect of controlled rolling just after cooling on mechanical properties, *ISIJ Int.* 56 (2016) 294–302.  
<http://doi.org/10.2355/isijinternational.ISIJINT-2015-454>.
- [18] C.F. Gomez, C.W.Mvd Geld, J.G.M. Kuerten, M. Bsibsi, B.P.Mv Esch, Quench cooling of fast moving steel plates by water jet impingement, *Int. J. Heat Mass Transf.* 163 (2020).  
<https://doi.org/10.1016/j.ijheatmasstransfer.2020.120545>,  
<http://www.ncbi.nlm.nih.gov/pubmed/120545>.
- [19] S.J. Chen, J. Kothari, A.A. Tseng, Cooling of a moving plate with an impinging circular water jet, *Exp. Therm. Fluid Sci.* 4 (1991) 343–353. [https://doi.org/10.1016/0894-1777\(91\)90051-R](https://doi.org/10.1016/0894-1777(91)90051-R).
- [20] A.K. Sharma, S.K. Sahu, The thermal and rewetting behavior of hot moving surface by water jet impingement, *Appl. Therm. Eng.* 159 (2019).  
<https://doi.org/10.1016/j.applthermaleng.2019.113950>,  
<http://www.ncbi.nlm.nih.gov/pubmed/113950>.
- [21] H. Fujimoto, Y. Shiramasa, K. Morisawa, T. Hama, H. Takuda, Heat transfer characteristics of a pipe-laminar jet impinging on a moving hot solid, *ISIJ Int.* 55 (2015) 1994–2001.  
<https://doi.org/10.2355/isijinternational.ISIJINT-2015-124>.

- [22] K. Morisawa, J. Nakahara, K. Nagata, H. Fujimoto, T. Hama, H. Takuda, Boiling heat transfer characteristics of vertical water jet impinging on horizontally moving hot plate, *ISIJ Int.* 58 (2018) 140–145. <https://doi.org/10.2355/isijinternational.ISIJINT-2017-383>.
- [23] F.P. Incropera, D.P. DeWitt, *Fundamentals of Heat and Mass Transfer*, John Willey and Sons, New York, 6, p. 116, 1996.
- [24] D.T. Vader, F.P. Incropera, R. Viskanta, A method for measuring steady local heat transfer to an impinging liquid jet, *Exp. Therm. Fluid Sci.* 4 (1991) 1–11. [https://doi.org/10.1016/0894-1777\(91\)90016-K](https://doi.org/10.1016/0894-1777(91)90016-K).
- [25] B.P. Leonard, A stable and accurate convective modelling procedure based on quadratic upstream interpolation, *Comput. Methods Appl. Mech. Eng.* 19 (1979) 59–98. [https://doi.org/10.1016/0045-7825\(79\)90034-3](https://doi.org/10.1016/0045-7825(79)90034-3).
- [26] J. Wang, N. Zabaras, A Bayesian inference approach to the inverse heat conduction problem, *Int. J. Heat Mass Transf.* 47 (2004) 3927–3941. <https://doi.org/10.1016/j.ijheatmasstransfer.2004.02.028>.
- [27] U.Z. Ijaz, A.K. Khambampati, M.C. Kim, S. Kim, K.Y. Kim, Estimation of time-dependent heat flux and measurement bias in two-dimensional inverse heat conduction problems, *Int. J. Heat Mass Transf.* 50 (2007) 4117–4130. <https://doi.org/10.1016/j.ijheatmasstransfer.2007.02.037>.

- [28] J. Taler, W. Zima, Solution of inverse heat conduction problems using control volume approach, *Int. J. Heat Mass Transf.* 42 (1999) 1123–1140. [https://doi.org/10.1016/S0017-9310\(98\)00280-4](https://doi.org/10.1016/S0017-9310(98)00280-4).
- [29] F. Bozzoli, G. Pagliarini, S. Rainieri, Experimental validation of the filtering technique approach applied to the restoration of the heat source field, *Exp. Therm. Fluid Sci.* 44 (2013) 858–867. <https://doi.org/10.1016/j.expthermflusci.2012.10.002>.
- [30] A.A. Ranjbar, M. Mirsadeghi, An inverse estimation of initial temperature profile in a polymer process, *Polym. Eng. Sci.* 48 (2008) 133–140. <https://doi.org/10.1002/pen.20930>.
- [31] C. de Boor, *A Practical Guide to Splines*, Springer, New York, 2001.